Phosphorus-Enhanced and Calcium-Retarded Transport of Ferrihydrite Colloid : Mechanism of Electrostatic Potential Changes Regulated via Adsorption Speciation

Environmental Science and Technology

Ma, Jie; Li, Jinbo; Weng, Liping; Ouyang, Xiaoxue; Chen, Yali et al

https://doi.org/10.1021/acs.est.2c09670

This publication is made publicly available in the institutional repository of Wageningen University and Research, under the terms of article 25fa of the Dutch Copyright Act, also known as the Amendment Taverne. This has been done with explicit consent by the author.

Article 25fa states that the author of a short scientific work funded either wholly or partially by Dutch public funds is entitled to make that work publicly available for no consideration following a reasonable period of time after the work was first published, provided that clear reference is made to the source of the first publication of the work.

This publication is distributed under The Association of Universities in the Netherlands (VSNU) 'Article 25fa implementation' project. In this project research outputs of researchers employed by Dutch Universities that comply with the legal requirements of Article 25fa of the Dutch Copyright Act are distributed online and free of cost or other barriers in institutional repositories. Research outputs are distributed six months after their first online publication in the original published version and with proper attribution to the source of the original publication.

You are permitted to download and use the publication for personal purposes. All rights remain with the author(s) and / or copyright owner(s) of this work. Any use of the publication or parts of it other than authorised under article 25fa of the Dutch Copyright act is prohibited. Wageningen University & Research and the author(s) of this publication shall not be held responsible or liable for any damages resulting from your (re)use of this publication.

For questions regarding the public availability of this publication please contact openscience.library@wur.nl

Environmental Science & Technology

pubs.acs.org/est

Article

Phosphorus-Enhanced and Calcium-Retarded Transport of Ferrihydrite Colloid: Mechanism of Electrostatic Potential Changes Regulated via Adsorption Speciation

Jie Ma,*,¶ Jinbo Li,¶ Liping Weng,* Xiaoxue Ouyang, Yali Chen, and Yongtao Li

Cite This: *Environ. Sci. Technol.* 2023, 57, 4219−4230

Read Online

ACCESS | Metrics & More | Article Recommendations | SI Supporting Information

ABSTRACT: The transport of ferrihydrite colloid (FHC) through porous media is influenced by anions (e.g., PO_4^{3-}) and cations (e.g., Ca^{2+}) in the aqueous environment. This study investigated the cotransport of FHC with P and P/Ca in saturated sand columns. The results showed that P adsorption enhanced FHC transport, whereas Ca loaded onto P−FHC retarded FHC transport. Phosphate adsorption provided a negative potential on the FHC, while Ca added to P-FHC led to electrostatic screening, compression of the electric double layer, and formation of $Ca_5(PO_4)_3OH$ followed by heteroaggregation at pH ≥ 6.0. The monodentate and bidentate P surface complexes coexisted, and Ca mainly formed a ternary complex with bidentate P ($\equiv(FeO)_2PO_2Ca$). The unprotonation bidentate P at the Stern 1-plane had a considerable negative potential at the Van der Waals molecular surface. Extending the potential effect to the outer layer of FHC, the potential at the Stern 2-plane and zeta potential exhibited a corresponding change, resulting in a change in FHC mobility, which was validated by comparison of experimental results, DFT calculations, and CD-MUSIC models. Our results highlighted the influence of P and Ca on FHC transport and elucidated their interaction mechanisms based on quantum chemistry and colloidal chemical interface reactions.

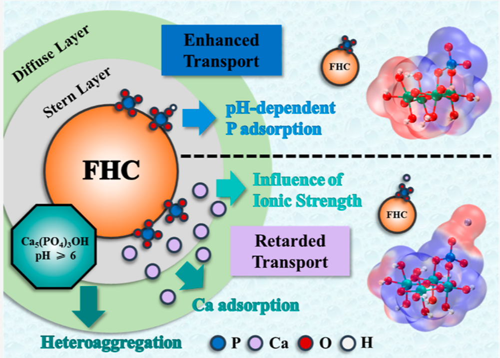

KEYWORDS: *ferrihydrite colloids, phosphorus, calcium, transport, CD-MUSIC, DFT calculation*

INTRODUCTION

Ferrihydrite (FH), a poorly crystalline oxide mineral, occurs naturally in water and hydromorphic soils and possesses a vast surface area and large amounts of reactive hydroxyl sites, which can regulate, scavenge, and transform contaminants.[1,2] Owing to the small size of individual nanocrystals, ferrihydrite colloids (FHCs) can transport over long distances in the vadose and aquifer.[3−5]

Numerous studies have focused on the stability and transport of FHC.[3−9] Humic acid (HA) has been identified as a crucial factor for safeguarding stability and promoting transport as it introduces a negative charge onto FHC.[4−6,8,9] High loading of a negative charge on the colloid- or nanoparticle-improved dispersion owing to electrostatic repulsion.[10,11] Previous studies reported that the presence of phosphate anions facilitated the transport of nano-ZVI and TiO_2 nanoparticles.[12,13] Similar to HA, the adsorption of anions (P) may also change the surface charge of iron minerals, such as FHC, which could eventually enhance their transport.

Phosphorus fertilizers are essential nutrients for crop growth. In a planting season, the rate of P-utilization by crops is generally 10−20%,[14−16] and the rest is associated with soil minerals.[17] According to studies, the adsorption and transport of P were primarily influenced by iron minerals.[18−24] Moreover, amorphous forms of Fe comprise the major fraction of medium-sized colloidal P.[25] Phosphate anions form inner-sphere and outer-sphere complexes via ligand exchange reactions and electrostatic interactions on the surface of Fe minerals,[26−28] resulting in a change in their surface charge. Apart from HA, P adsorption also influenced the change in potential in the Stern layer. The phenomenon did not only occur in the inner-sphere but also expanded to the outer-sphere, and FHC stability also benefited from it.[29,30] However, the effect of P on FHC transport requires further investigation.

In nature, P adsorption onto Fe minerals is affected by several factors. Adsorption typically decreases with increasing pH.[31−35] Moreover, compared with Na and K, Ca is a more critical factor owing to its strong reactivity with P. A previous study suggested a strong interaction between adsorbed Ca and PO_4^{3-} on Fe minerals under conditions below the saturation index of apatite.[36] For Ca and PO_4^{3-} adsorbed onto FHC, two anion-bridged ternary complexes, $\equiv(FeO)_2PO_2Ca$ and $\equiv$

Received: December 22, 2022
Revised: February 8, 2023
Accepted: February 10, 2023
Published: February 27, 2023

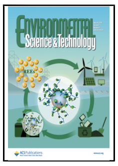

$FeOPO_3Ca$, were formed, depending on the relative binding affinities of the co-adsorbing ions.[34] Along with adsorption, precipitation associated with Ca at a high pH may be an essential mechanism by which P is immobilized.[37] Although there is some progression on the mathematical modeling of particle transport and cotransport with contaminants,[38−42] past research has not established a relationship between surface chemical transition and the transport of iron mineral nanoparticles.

The charge distribution and multi-site complexation (CD-MUSIC) model, an advanced surface complexation model, was developed to quantify ion adsorption onto metal (hydr)-oxides.[43] This surface complexation model not only contributes to the environmental assessment of elements but also advances our understanding of factors and mechanisms controlling the environmental behavior of elements. Previous studies have successfully predicted the adsorption of P and Ca on metal oxide surfaces through the CD-MUSIC model.[31,44−46] However, this model has not been used to analyze anion-facilitated nanoparticle transport. The adsorption of P and Ca onto iron minerals, such as FHC, results in forming monodentate or bidentate surface complexes, anion-bridged ternary complexes, with various protonation degrees.[31,34,36,43] Moreover, the complicated speciation of FHC under the influence of P and Ca causes multifarious changes in the electrostatic potential (ESP) profiles at the FHC surface. Recent density functional theory (DFT) advancements have facilitated calculating changes in ESP profiles.[47] However, the mechanism by which this change affects the potential of electrical double layers (EDLs) and, therefore, influences FHC transport remains undetermined.

Ferrihydrite colloids have been recognized as one of the critical substances in the natural environment. Their presence certainly coexisted with P and Ca owing to P-utilization globally and abundant Ca in nature; thus, their fate merits an in-depth investigation. This study investigated the influence of P and Ca on the transport of FHC in porous media. The mechanism underlying the interfacial interaction among FHC, P, and Ca was characterized via column experiments in combination with transport simulation, Derjaguin−Landau−Verwey−Overbeek (DLVO) theory, CD-MUSIC modeling, and ESP analysis. The results of this study can improve our understanding of anion-facilitated colloid transport.

■ MATERIALS AND METHODS

Preparation of FHC. Ferrihydrite was prepared by titrating dissolved $Fe(NO_3)_3{\cdot}9H_2O$ (Sinopharm Chemical Reagent Co. Ltd.) with NaOH to a pH of 7.5.[48] The X-ray diffraction (XRD) pattern of the solid, verifying the synthesized FH, is illustrated in the Supporting Information in Figure S1. Briefly, the FHC suspension was prepared by adding 1.0 g FH to 500 mL of Milli-Q water, followed by stirring and sonication. After settling for 24 h, the suspension was recovered via siphoning.[4,6,49] Scanning electron microscopy (SEM) images of the FHC are shown in Supporting Information, Figure S2; their micro-morphology is ellipsoidal. Because the experiments were conducted immediately after the preparation of the FHC suspension, the transformation of the FHC did not occur over a short period.[49] The concentrations of the FHC were determined by measuring the Fe content using atomic absorption spectroscopy (AAS, AAnalyst 900T, PerkinElmer) after dissolution with 6 M HCl.

Column Experiments. Column experiments were performed using 10 cm long glass chromatographic columns with an inner diameter of 1.5 cm. The columns were wet-packed with clean quartz sand (337.5 μm). The bulk density and effective porosity of the packed sand were 1.45 ± 0.02 $g{\cdot}cm^{-3}$ and 0.46 ± 0.03 $cm^3{\cdot}cm^{-3}$, respectively. After packing, the columns were pre-conditioned with approximately 15 pore volumes (PVs) of 1 mM NaCl in Milli-Q water using a peristaltic pump (BT-100 1F, Longer) in the up-flow mode. The rate of FHC deposition for the up-flow mode was greater than that for the down-flow mode.[38] In all column experiments, 10 PVs of 25 mg L^{-1} FHC at different pH, P concentrations, and $CaCl_2$ concentrations were injected into the columns, followed by elution with 5 PVs of Milli-Q water with the corresponding pH and ionic strength (IS, $CaCl_2$) at a constant Darcy velocity of 0.568 $cm{\cdot}min^{-1}$. The experimental conditions are listed in Supporting Information, Table S1.

The FHC concentrations in the effluent were measured at each PV using AAS after dissolution with 6 M HCl. The particle size and ζ potential of the FHC and ζ potential of the sand were measured using a dynamic light scattering analyzer, and the results are summarized in Supporting Information, Table S2. The P concentrations in the effluent were measured at each PV using inductively coupled plasma optical emission spectrometry (ICP-OES, Optima 5300DV, PerkinElmer). Following the completion of transport experiments, the sand in the columns was segmented into four 2.5 cm thick layers to analyze FHC and P retention. The deposition of FHC at the entrance of the column (0−2.5 cm) in certain treatments was observed via SEM using energy-dispersive spectroscopy (EDS) mapping (Merlin Compact, Zeiss).

Adsorption Experiments. Adsorption isotherms were obtained through batch adsorption experiments at pH 4−9. Three series of 25 mg L^{-1} FHC and 20 mg L^{-1} P were used with 0, 1, or 10 mM $CaCl_2$, respectively. The pH of the suspensions was adjusted by adding appropriate amounts of 10−100 mM HCl and NaOH. All adsorption experiments were performed in gas-tight 50 mL polyethylene centrifuge tubes (20 mL of suspension), and N_2 was added into all the solutions to minimize the influence of CO_2. The samples were equilibrated on a horizontal shaker at 25 ± 1 °C for 3 days. The final pH of the unfiltered suspension was measured using a pH meter. The suspension was centrifuged at 10,000 rpm (∼15,000*g*) for 30 min and filtered through 0.1 μm filters (Tianjin Jinteng Experimental Equipment Co., Ltd). The concentrations of P and Ca in the filtrate were measured using inductively coupled plasma ICP-OES (Optima 5300DV, PerkinElmer). The chemical species of P and Ca and mineral structure in the solid phase of FHC in 20 mg L^{-1} P (pH = 8.0), 20 mg L^{-1} P and 10 mM $CaCl_2$ (pH = 4.0), and 20 mg L^{-1} P and 10 mM $CaCl_2$ (pH = 8.0) were investigated via X-ray photoelectron spectroscopy (XPS) (ESCALAB 250Xi, Thermo Scientific) and XRD (Ultima IV, Rigaku), respectively.

Model and Calculation. *Transport Model.* As the column, sand, and filling methods are consistent with those in the previous studies, the hydraulic characteristics of the column are cited directly instead of being monitored by a conservative tracer.[4] The transport data was simulated using the colloid transport model, which included two-site kinetic retention to quantify the particle transport and retention in the column experiments.[50,51] A convective-dispersive equation (CDE) was employed to describe the P transport. The details of the colloid transport and CDE models are illustrated in

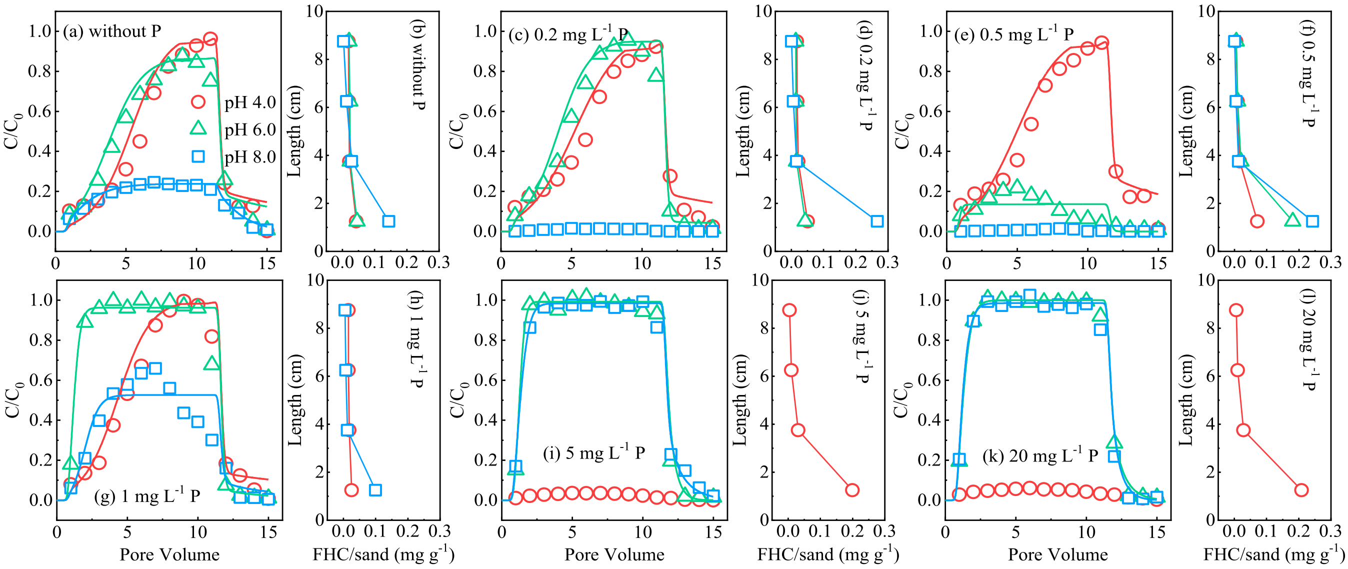

Figure 1. Breakthrough curves (BTCs) (a,c,e,g,i,k) and retention profiles (RPs) (b,d,f,h,j,l) of FHC in columns with different P concentrations (0–20 mg L^{-1}) at different pH. In the illustrated BTCs, symbols and solid lines indicate the observed data and simulation fitting, respectively. Data was not fitted with the FHC recovery (<10%) in the effluent. The FHC RPs were plotted as colloid retention per gram of dry sand as a function of distance from the column inlet. When FHC recovery in the effluent was higher than 95%, colloid retention in the column was not measured.

Supporting Information, S4 and S5. As a supplement, the particle size variations and molecular dynamics were investigated to study the homoaggregation of FHC and heteroaggregation between FHC and some reaction product, which may influence transport.[40]

DLVO Theory. The representative DLVO theory was used to calculate the total colloid–sand interaction energy by incorporating the Lifshitz–Van der Waals interactions to the EDL interactions.[52,53] The details of the DLVO theory and operative equations are presented in Supporting Information, S6. As the difference in colloidal particle size significantly affects the Van der Waals and electrostatic forces between colloid and sand, the particle size after adding the ions was used in calculations. In some cases, partial particle sizes were large owing to a low absolute value of ζ potential.

CD-MUSIC Model. Surface complexation on FHC was calculated using the CD-MUSIC model operated by ECOSAT software. The total concentrations of the added components and the measured pH were used as inputs in the model calculation, and the simulated P and Ca concentrations in the solution were compared with those measured. The details of the CD-MUSIC model and model parameters (Supporting Information, Table S3) are presented in Supporting Information S7.

DFT Calculation. For the simulations of different surface species formed after P adsorption onto the FHC based on the CD-MUSIC model, DFT calculations were performed using a Gaussian 16 software package.[54] The ESP was obtained using Visual Molecular Dynamics based on the output from the Multiwfn program.[55] The details of the DFT calculations are presented in Supporting Information, S8.

Molecular Dynamics Simulation. All the all-atom molecular dynamics (MD) simulations were based on a gromos54a7 force field[56] by Automated Topology Builder (ATB)[57] and were carried out using the Gromacs-2020.6 software package.[58] The details of the MD simulations are presented in Supporting Information, S9.

RESULTS AND DISCUSSION

Effect of P on FHC Transport. The observed and simulated results of FHC transport in sand columns and the DLVO energies between FHC and sand in the absence and presence of P are illustrated in Figure 1, Supporting Information, Figure S3 and Table S4. The normalized effluent concentrations of individual FHC were relatively low or moderate under all pH conditions (effluent recovery within 23.9–66.2%) (Figure 1a and Supporting Information, Table S4), which is similar to the results of our previous study.[4] The transport of FHC stabilized or decreased in the presence of P at low concentrations (0.2–0.5 mg L^{-1}), in which a decrease was more evident at pH 8.0, indicated by the meager recovery in the effluents (≤1.0%) (Figure 1c,e and Supporting Information, Table S4). The low amount of P decreased the positive potential of FHC to a value approaching 0, promoting homoaggregation, and thus decreased FHC transport.[4,8] The deposition of FHC yields hyperexponential retention profiles (Figure 1b,d,f,h,j,l) featuring a significant depth dependency.[50] The P-facilitated transport of FHC gradually emerged at pH 6.0 and 8.0 with increasing P concentrations (1–20 mg L^{-1}) and was indicated by the highest recovery rate in the effluents approaching 100% (Figure 1g,i,e and Supporting Information, Table S4). Phosphorus can be adsorbed by FHC owing to the reaction with the hydroxyl group;[46] thus, introducing a negative charge and sufficient P dramatically changed their ζ potentials to negative values on the surface of the FHC (Supporting Information, Table S2). Accordingly, the DLVO results showed that the primary energy barrier emerged (107.2–301.0 kT) (Supporting Information, Figure S3 and Table S4) and maintained the transport of FHC, except at pH 4.0. At a low pH, although the primary energy barrier is 175.5 kT in the presence of 20 mg L^{-1} P (Supporting Information, Table S4), the large particle size of FHC and low negative potential of sand were conducive to coagulation, filtration, straining, and deposition and thus, the large FHC was mostly retarded in the column.[4,5,7,8,49] The retention of FHC at pH 4.0 mainly occurred in reversible sites, corresponding to high

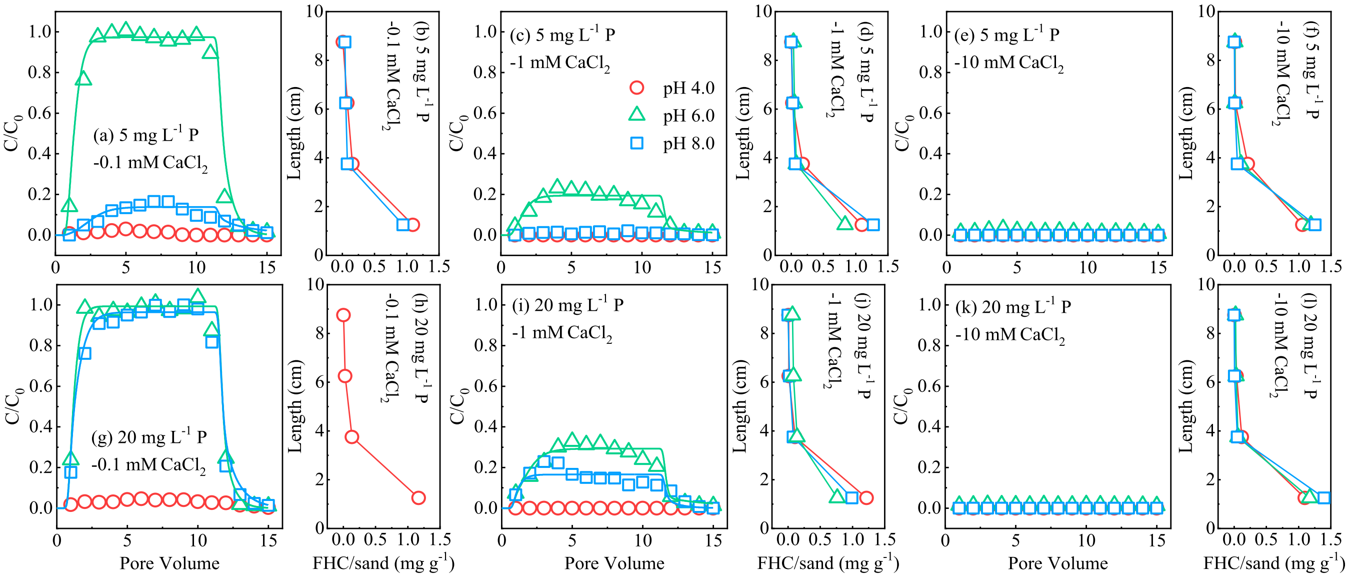

Figure 2. BTCs (a,c,e,g,i and k) and RPs (b,d,f,h,j and l) of FHC in columns with different P (5 and 20 mg L^{-1}) and CaCl$_2$ (0.1, 1, and 10 mM) concentrations at different pH. In the illustrated BTCs, symbols and solid lines indicate the observed data and simulation fitting, respectively. Data was not fitted with the FHC recovery (<10%) in the effluent. The FHC RPs were plotted as colloid retention per gram of dry sand as a function of distance from the column inlet. When FHC recovery in the effluent was higher than 95%, colloid retention in the column was not measured.

k_{1a} and low k_{2a} values (Supporting Information, Table S4). The values of k_{1d}/k_{1a} increased at pH 6.0 and 8.0 with increasing P concentrations, in which the values were proximate to or up to 1 in the presence of P at high concentrations (5 and 20 mg L^{-1}) (Supporting Information, Table S4), indicating that the high concentrations of P caused the reversible deposition of FHC to detach from the collector.[59] The change in the values of k_{1d}/k_{1a} and corresponding transport characteristics were similar to the data observed in dissolved organic matter, leading to the reduced deposition of other nanoparticles or colloids.[5,60−63]

Retardation Effect of Ca on P-FHC Transport. The breakthrough curves (BTCs) for the transport of FHC in the presence of P and Ca are illustrated in Figure 2, and the simulated results and DLVO energies are depicted in Supporting Information, Table S4 and Figure S4. At pH 4.0, considering the original low mobility of P-FHC, Ca further retarded their transport, and FHC was almost entirely deposited in the columns (92.9−99.6%) (Supporting Information, Table S4) regardless of the P and Ca concentrations. Similarly, the transport of FHC was retarded at neutral and alkaline pH, and the transport decreased (effluent recoveries decreased from 98.9−102.5% to 2.3−2.6%) with increasing Ca concentration (Figure 2 and Supporting Information, Table S4). Owing to the influence of divalent Ca ions on the ionic strength (IS) increment, the primary energy barriers under 10 mM Ca at pH 4.0 and 6.0 were considerably lower than those without Ca (Supporting Information, Figures S3 and S4 and Table S4). A much lower concentration of Ca^{2+} in the influent solution was required to yield a reduction in colloid transport than monovalent cations.[64]

Under the condition of 5 mg L^{-1} P at pH 6.0, when the Ca concentration increased from 0.1 to 1 mM, although the primary energy barriers slightly decreased from 168.1 to 158.9 kt (Supporting Information, Figure S4 and Table S4), FHC transport decreased dramatically, suggesting the presence of non-DLVO interactions. Moreover, the coexistence of P and Ca (1 and 10 mM) retarded FHC transport more significantly than Ca alone with corresponding concentrations at pH 4.0 and 6.0 (Figure 2 and Supporting Information, Figure S5). After P adsorption onto the FHC, the negative surface charge increased the affinity of the P-FHC for Ca, and two anion-bridged ternary complexes [$\equiv$(FeO)$_2$PO$_2$Ca and $\equiv$FeO-PO$_3$Ca] were formed.[34] The adsorption of Ca onto the P-FHC was inevitably embedded with a positive charge on the otherwise negatively charged surface, thereby increasing the heterogeneity of the FHC surface, which retarded FHC transport.

In the presence of P and Ca, the transport of FHC at pH 8.0 was retarded more significantly than that at pH 6.0 (Figure 2). For Ca concentrations ≥1 mM, FHC was resistant to transport out of the column (effluent recoveries: 0−17.8%) (Supporting Information, Table S4). The primary energy barriers at pH 8.0 decreased significantly compared with those without Ca (Supporting Information, Figures S3 and S4 and Table S4). In addition to the change in charge and heterogeneity, the reaction between phosphate and Ca contributes to the retardation at pH 8.0, and their coexistence at high pH yields calcium phosphate precipitates.[31,37] On the one hand, the precipitation reaction consumed P, which reduced the negative charge of the system; on the other hand, the generation of calcium phosphate precipitates increased the heteroaggregation with FHC.[6] Notably, these conditions were conducive to FHC deposition in the columns. Although the sand caused interference owing to its high silicon and oxygen content, randomly selected SEM−EDS points detected Ca signals under the cotransport of FHC, P, and Ca (Supporting Information, Figure S6). According to the DLVO theory, under the unfavorable attachment condition, large particles received strong electrostatic repulsion and thus readily transported out the columns (Supporting Information, Figure S7). However, owing to straining,[65] influent FHC with a large particle size (20 mg L^{-1} P−1 mM Ca pH 8.0, 1363.3 nm, Supporting Information, Table S2) was intercepted, and only the FHC with a small particle size (589.4−821.5 nm) in the

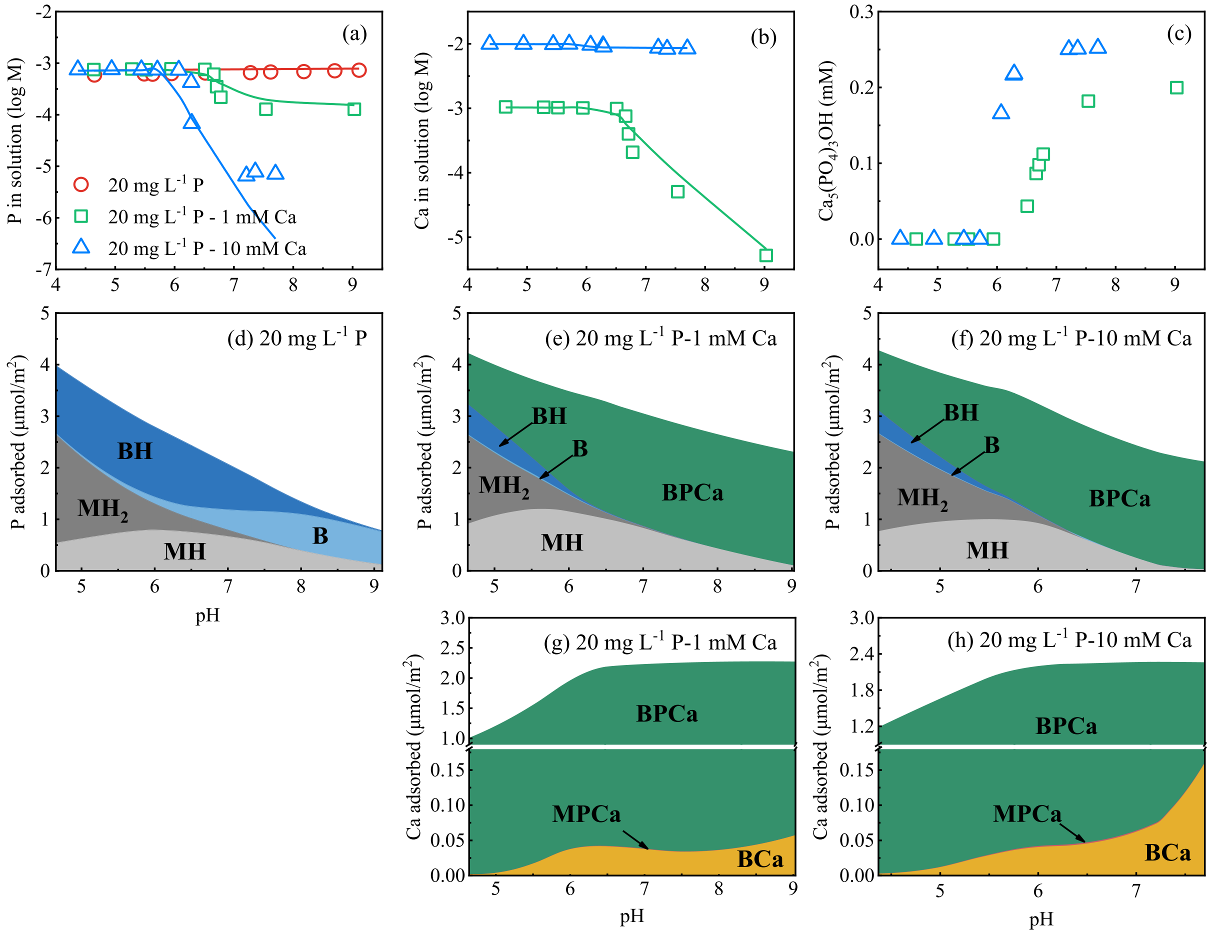

Figure 3. Adsorption envelopes of P (a) and Ca (b) onto FHC in the corresponding single- and binary-ion systems: the symbols represent experimental data, and the lines indicate CD-MUSIC model calculations. The amount of the pH-dependent formation of $Ca_5(PO_4)_3OH$ precipitate (CD-MUSIC model calculation) (c). pH-dependent surface speciation of P (d,e,f) and Ca (g,h) in the corresponding single- and binary-ion systems. For P: MH = monodentate protonated; MH_2 = monodentate doubly protonated; B = bidentate; and BH = bidentate protonated. For Ca: BCa = bidentate Ca at the low- and high-affinity sites. For the ternary species: MPCa = ternary complex with monodentate P−Ca; BPCa = ternary complex with bidentate P−Ca.

effluent were detected (Supporting Information, Figure S7). The retardation factor increased by an order of magnitude, indicating that precipitation and codeposition caused P retention (Supporting Information, Figure S8 and Table S5). Moreover, the P retention was positively correlated with FHC retention, and the pH and Ca concentration determined the slope of this correlation (Supporting Information, Figure S9). In addition, the contribution of Ca concentrations to P retention at pH 8.0 was relatively weak, as demonstrated by the similarity of the slopes (0.739 for the 1 mM Ca system, and 0.669 for the 10 mM Ca system) (Supporting Information, Figure S9). The intricate cotransport and codeposition suggested interactions between the P, Ca, and pH, influencing the FHC transport.

Adsorption and Speciation of P and Ca on FHC. The microinterface mechanism of P and Ca loading onto the surface of FHC was investigated via adsorption experiments. The P and Ca adsorption envelopes at different pH values, CD-MUSIC model fitting results, and surface speciation of adsorbed ions are depicted in Figure 3. The adsorption quantity decreased with increasing pH, and similar observations have been reported in previous studies.[44,46] However, in the presence of Ca, the P concentration in the solution sharply decreased with increasing pH, at an initial pH of 6.7 and 5.8 in 1 (decreased from 76 to 16%) and 10 (decreased from 53 to 1%) mM Ca systems, respectively (Figure 3a). Similarly, the concentration of Ca exhibited a decreasing trend in the 1 mM Ca system; however, it decreased slightly (up to ∼1.25 mM) in the 10 mM Ca system owing to its excess amount (Figure 3b). The decreasing tendency of P and Ca in the solution at relatively high pH indicates the formation of P and Ca precipitates.[31,66] The calcium phosphate precipitates, i.e., $Ca_2PO_4(OH)\cdot 2H_2O$ and $Ca_5(PO_4)_3OH$ with solubility products ($\log K_{so}$) of −18.9 and −53.3, respectively, were considered in the model calculation. The modeling results indicated that the less soluble $Ca_5(PO_4)_3OH$ was formed in the P and Ca coexistence systems (Figure 3c).

For individual P adsorption, monodentate and bidentate P surface complexes coexisted, and protonation likely occurred at low pH (Figure 3d). The presence of Ca increased P adsorption on FHC, which is attributed to the electrostatic synergy between PO_4^{3-} and Ca^{2+} at a relatively high pH.[67] Furthermore, Ca decreased the bidentate P surface complexes (B, BH) owing to the formation of ternary complexes (Figure 3e,f), the dominant bidentate ternary complex (BPCa), and the negligible monodentate ternary complex (MPCa) (Figure 3g,h). Moreover, the proportion of Ca directly adsorbed to FHC (BCa) was extremely low (Figure 3g,h). Minor

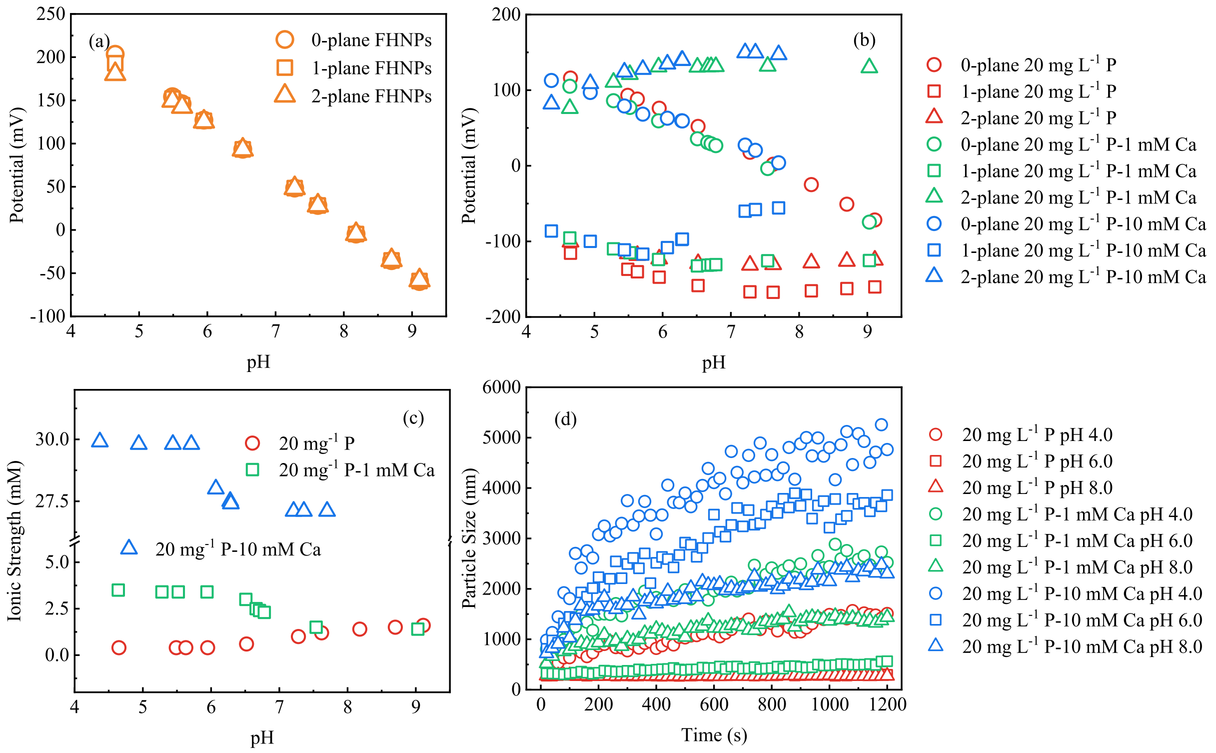

Figure 4. pH-dependent Stern plane potentials (0-plane, 1-plane, and 2-plane) of FHC (a) in single ion (P) and binary ion (P and Ca) systems (b) and ionic strength (c) in the corresponding systems (CD-MUSIC model calculation), and ζ potential (measurement) of FHC in the corresponding systems (a,b). Aggregation profiles of FHC (d).

differences were observed in the speciation of monodentate P (MH and MH_2) in the absence and presence of Ca.[34]

The XRD and XPS results affirmed the speciation of the elements derived from adsorption modeling, especially precipitation formation. Although other peaks were overspread, XRD spectra of 2-line FH were observed in all samples (approximately 35° and 62°)[68] (Supporting Information, Figure S10a). $Ca_5(PO_4)_3OH$ was present in the solid phase in the presence of Ca at pH 8.0, corresponding to the standard spectrum (PDF 89-4405),[69] and extremely trace amounts of $Ca_5(PO_4)_3OH$ were detected at pH 4.0 (Supporting Information, Figure S10a). This supported the formation of precipitation of this mineral predicted in the CD-MUSIC modeling. Moreover, the XPS spectrum results demonstrated that different amounts of P and Ca were loaded onto FHC (Supporting Information, Figure S10a), and the ratio of Fe, P, and Ca calculated in the CD-MUSIC modeling was similar to that from the XPS results (Supporting Information, Table S6). When P and Ca coexisted at a high pH, the Ca 2p peaks were extremely high and smooth (Supporting Information, Figure S10i), implying that the reaction between Ca and P results in the formation of $Ca_5(PO_4)_3OH$ precipitation. A blue shift was observed under 20 mg L^{-1} P at pH 8.0 and 20 mg L^{-1} P−10 mM $CaCl_2$ at pH 4.0 (Supporting Information, Figure S10d,g), suggesting that P formed stable inner sphere complexes[28] rather than precipitation. Notably, an apparent increase in the relative intensity of the $Ca_5(PO_4)_3OH$, P−O, and O−P(O−H) peaks was observed, which arose from the lack of Ca participation at high pH. This result suggested that the CD-MUSIC model results were accurate.

Effect of Adsorption of P and Ca on FHC Transport. Although the time required for adsorption experiments (3 days for achieving complete equilibrium) was greater than that required for transport experiments (approximately 2 h), considering that P adsorption reactions are fast processes occurring within a few minutes, the results of adsorption modeling could sufficiently explain the transport experiment.[70] Notably, the surface potentials of P- and P/Ca-loaded FHC changed. Conceptually, all atoms were located in the inner Stern layer region (0- and 1-plane) after P adsorption,[34,71] causing a constant negative potential (−115.7 to −167.4 mV) of the 1-plane at different pH (Figure 4b). Moreover, at different pH values, the potential of the 0-plane decreased compared with that of clean FHC owing to the formation of the P complex (Figure 4a,b). Although the phosphate radical did not physically enter the outer Stern layer region (2-plane), the potential of the 2-plane was negative (−100.8 to −131.5 mV), suggesting that P adsorption caused potential changes featuring spatial expansibility. Moreover, because part of the ternary complex might physically enter the 2-plane,[34] the positive charges existed on the 2-plane (Figure 4b). In the 10 mM Ca system, a certain amount of BPCa (Figure 3h) neutralized part of the negative charge at the 1-plane, which was generated by P adsorption, especially at high pH (Figure 4b). Overall, sufficient P adsorption decreased the Stern plane potentials of FHC to a negative value, and the formation of BPCa subsequently rendered it positive. The absolute values of the Stern layer potentials remained higher than those of the ζ potentials (Figure 4b), which is consistent with the rule that the potential decreases with distance from the colloids. However, overall, the potential changes in the EDL were regulated via the adsorption of P and Ca, which further controlled FHC transport.

Owing to adsorption, the IS of the solution decreased compared to that of the pristine solution (Figure 4c), which is favorable for FHC transport. However, divalent Ca ions

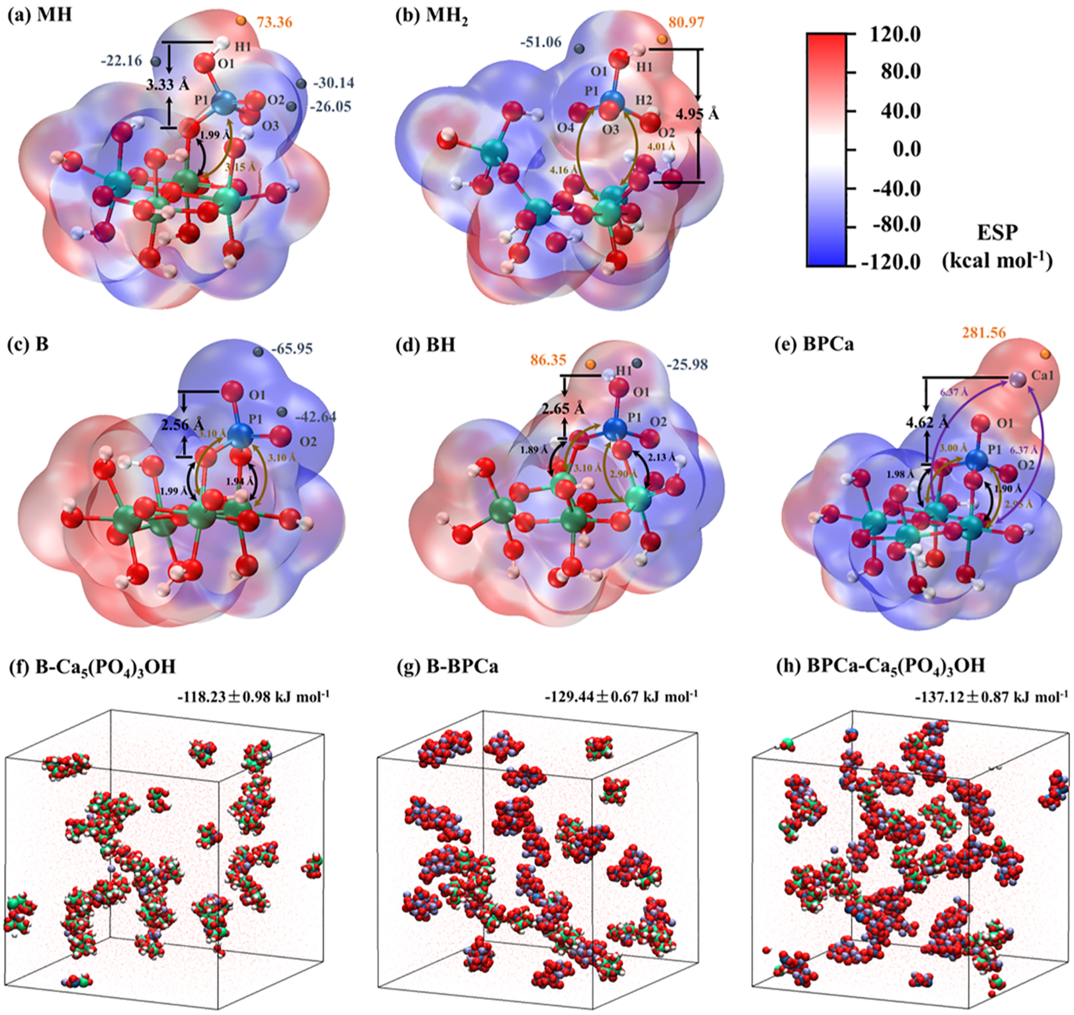

Figure 5. ESP-mapped molecular Van der Waals surface of different speciation of adsorbed P and Ca (a−e). MD simulations of B−$Ca_5(PO_4)_3OH$, B−BPCa, and BPCa−$Ca_5(PO_4)_3OH$ (f−h). The green, red, white, and violet spheres represent Fe, O, H, and Ca, respectively. Ball-stick and Van der Waals ball represent atoms in ESP and MD simulations, respectively. The surface local minima and maxima of ESP related to phosphate radicals and Ca are represented as dark blue and orange spheres, respectively. ESP indicates the electrostatic potential of the macromolecule, wherein red and blue are the positive and negative areas, respectively. Key atomic distances and unbonded atoms with the FH (characteristics of the electrostatic potential of atoms are shown in Supporting Information, Table S7) have been marked.

contribute greatly to the IS; thus, in the 10 mM Ca system, the IS dominated the retardation of FHC transport by promoting deposition and homo(hetero)aggregation (Figure 4d). The types of aggregation may divide by ∼ pH 6.0, with homoaggregation between the P/Ca-loaded FHC predominating at low pH and heteroaggregation predominating between the P/Ca-loaded FHC and generated $Ca_5(PO_4)_3OH$ at high pH. Homo(hetero)aggregation affected FHC attachment onto the collector.[40] Consequently, FHC barely transported out of the column (Figure 2k), regardless of aggregate types. In the 1 mM Ca system, although the IS decreased at high pH values (Figure 4c), FHC transport slightly improved compared to that in the 10 mM Ca system. This further confirmed that the formation of $Ca_5(PO_4)_3OH$ featured a positive charge (Supporting Information, Figure S11) and promoted heteroaggregation (Figure 4d), especially at alkaline pH. The bridging effect of Ca and P may enhance homo(hetero)-aggregation. This caused straining of FHC in the columns, further leading to a decrease in the particle size in the effluent (Supporting Information, Figure S7).

Furthermore, CD-MUSIC model calculations were conducted for other transport experimental conditions, which were not performed in the adsorption experiment, and the results are illustrated in Supporting Information, S18. Although no inverse iteration was performed on the adsorption experimental data, the CD-MUSIC model calculations agreed with the inverse results based on adsorption experiments (Figures 3, 4 and Supporting Information, S12−S15). For P concentrations greater than 1 mg L^{-1}, the Stern potentials of the 1-plane and 2-plane were negative at pH > 5.0 (Supporting Information, Figure S13c,d). This corresponded well with the characteristics of ζ potential (Supporting Information, Table S2) and the negative potential promoted transport (Figure 1g,i) at these P concentrations. Ca increased the Stern potential of the 2-plane to positive values (Supporting Information, Figure S13e−h), directly affecting the ζ potential, which is a defining characteristic of transport. Although the changes in IS caused via adsorption were moderate (Supporting Information, Figure S14), radical alteration in the FHC transport was limited. Notably, the primary speciation of adsorbed P and Ca (Supporting Information,

Figure S15) and the difference in potential changes in EDL and transport should be detailed further.

Effect of P Speciation on Electrostatic Potential Profiles and Aggregation of FHC. Although changes in ζ and Stern potentials after P adsorption were well defined, the electrostatic potential profiles affected by speciations of adsorbed P required further investigation. Moreover, in the CD-MUSIC model, both charge and potential are assumed to be uniformly distributed, which is inconsistent with the real situation. Based on the CD-MUSIC model results, we performed DFT calculations for five major species of adsorbed P and Ca (MH, MH_2, B, BH, and BPCa), and their ESP. The ESP-mapped Van der Waals surface and the surface extrema of different speciations of adsorbed P and Ca are depicted in Figure 5. Owing to the instability of the FH crystal, in some clusters, chemical bonds on FH were broken (Figure 5b,d). Therein, the MH_2 species was an outer−sphere complex, similar to the results of the previous DFT calculations.[28] The important Fe−O, Fe−P, and Fe−Ca distances were in the ranges of 1.90−2.13, 2.95−4.16, and 6.37 Å (Figure 5), respectively, which are similar to those obtained via other DFT calculations and synchrotron radiation experimental results.[34,35,72]

The local regional electrostatic potential areas of unbonded H, O, and Ca atoms with the FH cluster are listed in Supporting Information, Table S7. After P and Ca adsorption, the surface electrical properties of the interface of the P-(P/Ca-)related part in the FH cluster were mainly altered, whereas the changes in other parts calculated were not considered for the study of the colloid transport. Therefore, we solely focused on the P-(P/Ca-)related part. Phosphate possesses O atoms as well as negative charges. The coordinate and protonated O occupies their octet group, whereas the unprotonated O is highly electronegative. Accordingly, the atomic orbitals (expressed as electron probability density or wave functions) of this unprotonated oxygen in the P−FH cluster participate in the molecular orbitals and adjust their electronegativity.[73] According to the ESP results of different clusters obtained via wave function analysis, the extreme point potential affected by H, O, and Ca (P-(P/Ca-)related part) was −65.95 to 281.56 kcal mol^{-1} (Figure 5). In the B species, the extreme point potentials were minimum values (−65.95 and −42.64 kcal mol^{-1}) and all areas of the local Van der Waals surface of unbonded O exhibited negative electrostatic potential (Figure 5c and Supporting Information, Table S7). Once the O was protonated, maxima appeared and their absolute values were higher than nearby minima (Figure 5). However, overall, the area of negative electrostatic potential (ANEP, 51.9−68.8%) was wider than the area of positive electrostatic potential (APEP, 31.2−48.1%) in the protonated species, and the unprotonated O contributed greatly to the ANEP (Supporting Information, Table S7). Although protonation decreased the electronegativity of the P-related part, the negative potential still had the advantage on the distribution area. The presence of Ca dramatically changed the potential of the prominent part, and the positive potential (59.2%) was dominant (Figure 5e and Supporting Information, Table S7).

In the absence of Ca, the distance between the outermost atom of phosphate radical and the surface of the FH cluster (O atom) was 2.56−4.95 Å. Most of the atoms of phosphate radical were within the 1-plane in the Stern layer (4.0 Å) defined by the CD-MUSIC model. The larger electronegativity generated by unprotonated bidentate P adsorption was more favorable for positively charged Ca loading. The Ca−O distance was 4.62 Å within a 2-plane in the Stern layer (4.0−8.0 Å). Previous quantum chemistry-related studies reported that P and Ca co-adsorption on FHC surfaces formed a cluster configuration of the inner-layer P and outer-layer Ca.[34] Thus, the positively charged Ca ions shielded the negative charges generated via P adsorption. Although the outer-layer Ca exhibited a strong positive potential, the O of the inner-layer phosphate radical still showed a negative potential (Figure 5e and Supporting Information, Table S7). The CD-MUSIC model results confirmed this inference, shown in this study and previous studies.[34]

We selected the P species of B with the highest electronegativity, BPCa with the highest electropositivity, and $Ca_5(PO_4)_3OH$ crystal for MD simulations to study their aggregation. At the end of the simulations, most of the molecular clusters aggregated, and many small aggregates were present in the final configuration. Theoretical calculations evaluating the binding energies between them were presented in the order of B−$Ca_5(PO_4)_3OH$ (−118.2 ± 1.0 kJ mol^{-1}) < B−BPCa (−129.4 ± 0.7 kJ mol^{-1}) < BPCa−$Ca_5(PO_4)_3OH$ (−137.1 ± 0.9 kJ mol^{-1}), which were equivalent to −47.75, −52.28, and −55.38 kT, respectively. These stable P species confirmed by the DFT and CD-MUSIC models could aggregate easily. Although these attractive interactions were much shallower than primary minimum interactions, their magnitudes are comparable to primary minimum interactions when charge heterogeneities are considered.[74] The binding energy between the negatively charged B and positively charged BPCa was lower than that between BPCa and $Ca_5(PO_4)_3OH$, suggesting that the non-DLVO interactions were more significant than the electrostatic interaction. Moreover, in the presence of calcium and at high pH, heteroaggregation had a strong influence on FHC transport. Because binding energies between molecular clusters were much higher than the second minimum energy, once colloids deposited on the predeposited $Ca_5(PO_4)_3OH$ or BPCa, the non-DLVO interactions might help colloids resist the flow shear force. These non-DLVO interactions were preferentially associated with pH-dependent speciation of P adsorption and reaction product, which were calculated using the DFT and CD-MUSIC models.

Although scale differences existed between quantum chemistry and surface complexation models, the results showing a negative potential in the Stern layer were consistent. Moreover, the quantum chemistry results further illustrated the effect of different P complexation on the potential change in the system. The correlation between the ANEP-APEP and charge distribution of surface species in the outermost charged plane (Supporting Information, Table S3) (R^2 = 0.744) (Supporting Information, Figure S16), implied that the DFT results were in agreement with the input parameters of CD-MUSIC model and confirmed that different adsorption structures led to different charged properties. In the CD-MUSIC model, the Stern potential of the 2-plane (Figures 4b and Supporting Information, Figure S13) was calculated based on the model results of surface species (Figures 3d−h and Supporting Information, Figure S15) and the charge distribution of surface species (Supporting Information, Table S3), considering the capacitance between planes (Supporting Information, S7).[75,76] Moreover, the positive correlations between ζ potential and Stern potential of the 2-plane (Supporting Information, Figure S17) suggested that the measurements and the results of the CD-MUSIC model matched well. The negative potential owing to P adsorption dropped somewhat linearly in the Stern layer (from 1-plane to 2-plane) and thereafter exponentially through the diffuse layer, approaching a zero value at the imaginary boundary of the EDL.[77] The positive correlations between ζ potential and Stern potential of the 2-plane in the single P systems seemed not to be affected by pH or P concentrations. However, quite remarkably, the exact position of the EDL is uncertain.[78] The charge screening induced by high P concentrations changed the EDL location and decreased prediction accuracy. Moreover, the results of a previous study suggested that under a high P loading, the particles generated a higher negative charge in the CD-MUSIC model results than the measured values.[78] This may indicate that the Stern potentials from the CD-MUSIC model were much higher than the measured ζ potentials in the present study. Overall, pH and P concentrations modulated the original P speciation and their ratios, further regulating Stern and ζ potentials, which eventually had substantial impacts on FHC transport.

The magnitude of the ζ potential of the colloids is also related to the thickness of the EDL, which is regulated via the IS. In the presence of Ca, the positive correlations between ζ potential and Stern potential of the 2-plane got progressively worse with increasing pH (Supporting Information, Figure S17e−h). On the one hand, this was affected by the IS of Ca; conversely, although the CD-MUSIC model was unable to calculate the potential contribution of generated $Ca_5(PO_4)_3OH$, according to the MD simulation, heteroaggregation of BPCa−$Ca_5(PO_4)_3OH$ and their deposition may lead to the substantial underestimation of the positive potential of measured values. Therefore, the correlations between measured values and model results were interfered, especially at high pH. The effect of electronegativity shielding, compression of the EDL, and precipitation at neutral and alkaline pH retarded FHC transport. The adsorption of P and Ca onto FHC and colloid transport were elucidated by DFT calculation, CD-MUSIC model, MD simulation, DLVO theory, and colloid transport model. In the natural environment, the NOM is present in abundance; thus, FHC is more likely to interact with NOM. The influence of NOM is equally important in the porous medium, which must be considered.

■ ENVIRONMENTAL IMPLICATIONS

Iron minerals, such as FH, are among the most active components in soil, and the activity of FHC with a strong transport ability is relatively prominent. Moreover, P is an important fertilizer abundant in agricultural soils, and Ca is present in high concentrations in the soil. Our findings highlighted the significant environmental implications of P and Ca in soils containing FHC. A previous study confirmed the close relationship between amorphous Fe colloids and P.[25] After conventionally applying P fertilizer in agricultural production, the P concentration in the soil pore water can be as high as 4−6 mg L^{-1}.[19] The concentration of dissolved reactive P approached 10.1−31.2 mg L^{-1} in grassland and forest soils.[79] In this case, abundant P in soils might cause the cotransport of P and FHC through the soil profile to groundwater. Previous studies have reported nanoparticle- or colloid-facilitated transport of contaminants,[42,80−84] including P;[25,85] however, in this study, P, as an oxyanion contaminant, facilitated the transport of colloids following inner-sphere adsorption. Conceptually, the role of P changed from a passenger to a driver in the transport. Additionally, under certain conditions, the carrier could adsorb other contaminants, leading to P-facilitated cotransport of multiple contaminants. A similar phenomenon was observed in a study on contaminants loaded with fine particle fractions of sediments in a river delta front estuary; reportedly, a positive correlation was observed between P and heavy metals, with r^2 values of 0.990 and 0.992 for As and Cd, respectively.[85] The hydrodynamics promoted the cotransport of contaminants via fine particles in the river, and the vadose and baseflow in the soil and aquifer may have achieved a similar result. In this study, Ca retarded the transport of P−FHC owing to the increase in IS, formation of a ternary complex with bidentate P, and precipitation of $Ca_5(PO_4)_3OH$; this retardation is likely to occur in calcareous soils. However, P-facilitated cotransport of multiple contaminants in low-Ca soils is of concern. Furthermore, other oxygen-containing anions, such as arsenate, chromate, and dichromate, are likely to exhibit similar abilities, thereby warranting further research and attention.

■ ASSOCIATED CONTENT

Supporting Information

The Supporting Information is available free of charge at https://pubs.acs.org/doi/10.1021/acs.est.2c09670.

> Ferrihydrite characteristics; column experiments condition; particle size and ζ potential of experimental material; colloid transport models; phosphorus transport models; DLVO theory; CD-MUSIC model; DFT calculation; molecular dynamics simulation; fitted parameters of FHC transport in the sand columns; DLVO interaction energy between FHC and sand; effect of Ca on FHC transport; codeposition of FHC with P and Ca; particle size of FHC in the effluent; phosphorus transport and deposition; information on XRD and XPS; ζ potential of $Ca_5(PO_4)_3OH$ precipitate; CD-MUSIC model calculations of adsorption of P and Ca onto FHC; characteristics of the electrostatic potential of atoms; and association among the DFT results, CD-MUSIC model, and ζ potential (PDF)

■ AUTHOR INFORMATION

Corresponding Authors

Jie Ma − *Key Laboratory for Environmental Factors Control of Agro-Product Quality Safety and Agro-Environmental Protection Institute, Ministry of Agriculture and Rural Affairs, Tianjin 300191, China*; orcid.org/0000-0003-3404-6544; Email: majie@caas.cn

Liping Weng − *Key Laboratory for Environmental Factors Control of Agro-Product Quality Safety and Agro-Environmental Protection Institute, Ministry of Agriculture and Rural Affairs, Tianjin 300191, China; Department of Soil Quality, Wageningen University, Wageningen 6700 AA, The Netherlands*; Email: wengliping@caas.cn

Authors

Jinbo Li − *Agro-Environmental Protection Institute, Ministry of Agriculture and Rural Affairs, Tianjin 300191, China; School of Grassland Science, Beijing Forestry University, Beijing 100083, China*

Xiaoxue Ouyang − *Institute of Agricultural Product Quality, Safety and Nutrition, Tianjin Academy of Agricultural Sciences, Tianjin 300381, China; Agro-Environmental*

Protection Institute, Ministry of Agriculture and Rural Affairs, Tianjin 300191, China

Yali Chen − *Key Laboratory for Environmental Factors Control of Agro-Product Quality Safety and Agro-Environmental Protection Institute, Ministry of Agriculture and Rural Affairs, Tianjin 300191, China*

Yongtao Li − *Agro-Environmental Protection Institute, Ministry of Agriculture and Rural Affairs, Tianjin 300191, China; College of Natural Resources and Environment, South China Agricultural University, Guangzhou 510642, China*

Complete contact information is available at: https://pubs.acs.org/10.1021/acs.est.2c09670

Author Contributions

¶J.M. and J.L. contributed equally to this study and should be regarded as the first joint authors.

Notes

The authors declare no competing financial interest.

■ ACKNOWLEDGMENTS

The study is financially supported by the National Natural Science Foundation of China (no. 41701262) and the National Key Research and Development Program of China (2016YFD0800102). The authors would like to thank Shiyanjia Lab (www.shiyanjia.com) for the DFT calculation and MD simulation and Jiayi Liu for polishing the English language.

■ REFERENCES

(1) Boily, J.-F.; Song, X. Direct identification of reaction sites on ferrihydrite. *Commun. Chem.* **2020**, *3*, 79.

(2) Wang, Y.; Newman, D. K. Redox reactions of phenazine antibiotics with ferric (hydr)oxides and molecular oxygen. *Environ. Sci. Technol.* **2008**, *42*, 2380−2386.

(3) Tosco, T.; Bosch, J.; Meckenstock, R. U.; Sethi, R. Transport of ferrihydrite nanoparticles in saturated porous media: role of ionic strength and flow rate. *Environ. Sci. Technol.* **2012**, *46*, 4008−4015.

(4) Qian, X.; Ma, J.; Weng, L.; Chen, Y.; Ren, Z.; Li, Y. Influence of agricultural organic inputs and their aging on the transport of ferrihydrite nanoparticles: From enhancement to inhibition. *Sci. Total Environ.* **2020**, *719*, 137440.

(5) Ma, J.; Guo, H. M.; Lei, M.; Li, Y. T.; Weng, L. P.; Chen, Y. L.; Ma, Y. L.; Deng, Y. X.; Feng, X. J.; Xiu, W. Enhanced transport of ferrihydrite colloid by chain-shaped humic acid colloid in saturated porous media. *Sci. Total Environ.* **2018**, *621*, 1581−1590.

(6) Ma, J.; Jing, Y.; Gao, L.; Chen, J.; Wang, Z.; Weng, L.; Li, H.; Chen, Y.; Li, Y. Hetero-aggregation of goethite and ferrihydrite nanoparticles controlled by goethite nanoparticles with elongated morphology. *Sci. Total Environ.* **2020**, *748*, 141536.

(7) Liao, P.; Yuan, S.; Wang, D. Impact of redox reactions on colloid transport in saturated porous media: An example of ferrihydrite colloids transport in the presence of sulfide. *Environ. Sci. Technol.* **2016**, *50*, 10968−10977.

(8) Liao, P.; Li, W.; Wang, D.; Jiang, Y.; Pan, C.; Fortner, J. D.; Yuan, S. Effect of reduced humic acid on the transport of ferrihydrite nanoparticles under anoxic conditions. *Water Res.* **2017**, *109*, 347−357.

(9) Gentile, L.; Wang, T.; Tunlid, A.; Olsson, U.; Persson, P. Ferrihydrite nanoparticle aggregation induced by dissolved organic matter. *J. Phys. Chem. A* **2018**, *122*, 7730−7738.

(10) Chen, Y.; Ma, J.; Li, Y.; Weng, L. Enhanced cadmium immobilization in saturated media by gradual stabilization of goethite in the presence of humic acid with increasing pH. *Sci. Total Environ.* **2019**, *648*, 358−366.

(11) Wang, D.; Jin, Y.; Jaisi, D. P. Effect of size-selective retention on the cotransport of hydroxyapatite and goethite nanoparticles in saturated porous media. *Environ. Sci. Technol.* **2015**, *49*, 8461−8470.

(12) Wang, Z.; Shen, C.; Du, Y.; Zhang, Y.; Li, B. Influence of phosphate on deposition and detachment of TiO2 nanoparticles in soil. *Front. Env. Sci. Eng.* **2019**, *13*, 79.

(13) Chen, M.; Xu, N.; Christodoulatos, C.; Wang, D. Synergistic effects of phosphorus and humic acid on the transport of anatase titanium dioxide nanoparticles in water-saturated porous media. *Environ. Pollut.* **2018**, *243*, 1368−1375.

(14) Holford, I. C. R. Soil phosphorus: its measurement, and its uptake by plants. *Soil Res* **1997**, *35*, 227−240.

(15) Sattari, S. Z.; Bouwman, A. F.; Giller, K. E.; van Ittersum, M. K. Residual soil phosphorus as the missing piece in the global phosphorus crisis puzzle. *P. Natl. Acad. Sci. USA* **2012**, *109*, 6348−6353.

(16) Yao, Z.; Wang, D.; Xu, N.; Du, C.; Feng, Y.; Qi, Y. Phosphate and humic acid inhibit corrosion of green-synthesized nano-iron particles to remove Cr(VI) and facilitate their cotransport. *Chem. Eng. J.* **2022**, *450*, 136415.

(17) Fang, H.; Cui, Z.; He, G.; Huang, L.; Chen, M. Phosphorus adsorption onto clay minerals and iron oxide with consideration of heterogeneous particle morphology. *Sci. Total Environ.* **2017**, *605-606*, 357−367.

(18) Lü, C.; Yan, D.; He, J.; Zhou, B.; Li, L.; Zheng, Q. Environmental geochemistry significance of organic phosphorus: An insight from its adsorption on iron oxides. *Appl. Geochem.* **2017**, *84*, 52−60.

(19) Ma, Y.; Ma, J.; Peng, H.; Weng, L.; Chen, Y.; Li, Y. Effects of iron, calcium, and organic matter on phosphorus behavior in fluvo-aquic soil: farmland investigation and aging experiments. *J. Soils Sediments* **2019**, *19*, 3994−4004.

(20) Celi, L.; Prati, M.; Magnacca, G.; Santoro, V.; Martin, M. Role of crystalline iron oxides on stabilization of inositol phosphates in soil. *Geoderma* **2020**, *374*, 114442.

(21) Alovisi, A. M. T.; Cassol, C. J.; Nascimento, J. S.; Soares, N. B.; da Silva Junior, I. R.; da Silva, R. S.; da Silva, J. A. M. Soil factors affecting phosphorus adsorption in soils of the Cerrado, Brazil. *Geoderma Reg* **2020**, *22*, No. e00298.

(22) Amini, M.; Antelo, J.; Fiol, S.; Rahnemaie, R. Modeling the effects of humic acid and anoxic condition on phosphate adsorption onto goethite. *Chemosphere* **2020**, *253*, 126691.

(23) Ma, J.; Ma, Y.; Wei, R.; Chen, Y.; Weng, L.; Ouyang, X.; Li, Y. Phosphorus transport in different soil types and the contribution of control factors to phosphorus retardation. *Chemosphere* **2021**, *276*, 130012.

(24) Chen, Y.; Huang, L.; Zhang, R.; Ma, J.; Guo, Z.; Zhao, J.; Weng, L.; Li, Y. Retardation factors in controlling the transport of inorganic, organic, and particulate phosphorus in fluvo-aquic soil. *Ecotox. Environ. Safe.* **2023**, *249*, 114402.

(25) Fresne, M.; Jordan, P.; Fenton, O.; Mellander, P. E.; Daly, K. Soil chemical and fertilizer influences on soluble and medium-sized colloidal phosphorus in agricultural soils. *Sci. Total Environ.* **2021**, *754*, 142112.

(26) Chitrakar, R.; Tezuka, S.; Sonoda, A.; Sakane, K.; Ooi, K.; Hirotsu, T. Phosphate adsorption on synthetic goethite and akaganeite. *J. Colloid Interface Sci.* **2006**, *298*, 602−608.

(27) Luengo, C.; Brigante, M.; Antelo, J.; Avena, M. Kinetics of phosphate adsorption on goethite: comparing batch adsorption and ATR-IR measurements. *J. Colloid Interface Sci.* **2006**, *300*, 511−518.

(28) Sudhakar, C.; Mukherjee, S.; Kumar, A. A.; Paramasivam, G.; Meena, P. K.; Nonappa; Pradeep, T. Interference of Phosphate in Adsorption of Arsenate and Arsenite over Confined Metastable Two-Line Ferrihydrite and Magnetite. *J. Phys. Chem. C* **2021**, *125*, 22502−22512.

(29) Wang, Z.; Ma, J.; Chen, Y.; Weng, L.; Gu, Y.; Li, Y. Stability of ferrihydrite and goethite nanoparticles under different environmental conditions. *Environ. Sci.* **2020**, *41*, 2292−2300.

(30) Ma, J.; Ma, Y.; Qian, X.; Wang, Z.; Chen, Y.; Weng, L.; Li, Y. Phosphorus adsorption onto ferrihydrite and predicting colloidal phosphorus transport. *Chinese Journal of Eco-Agriculture* **2021**, *29*, 85−93.

(31) Deng, Y.; Li, Y.; Li, X.; Sun, Y.; Ma, J.; Lei, M.; Weng, L. Influence of calcium and phosphate on pH dependency of arsenite and arsenate adsorption to goethite. *Chemosphere* **2018**, *199*, 617−624.

(32) Deng, Y.; Weng, L.; Li, Y.; Ma, J.; Chen, Y. Understanding major NOM properties controlling its interactions with phosphorus and arsenic at goethite-water interface. *Water Res.* **2019**, *157*, 372−380.

(33) Zhou, A.; Tang, H.; Wang, D. Phosphorus adsorption on natural sediments: modeling and effects of pH and sediment composition. *Water Res.* **2005**, *39*, 1245−1254.

(34) Mendez, J. C.; Hiemstra, T. Ternary complex formation of phosphate with Ca and Mg ions binding to ferrihydrite: Experiments and mechanisms. *ACS Earth Space Chem* **2020**, *4*, 545−557.

(35) Wang, X.; Li, W.; Harrington, R.; Liu, F.; Parise, J. B.; Feng, X.; Sparks, D. L. Effect of ferrihydrite crystallite size on phosphate adsorption reactivity. *Environ. Sci. Technol.* **2013**, *47*, 10322−10331.

(36) Rietra, R. P.; Hiemstra, T.; van Riemsdijk, W. H. Interaction between calcium and phosphate adsorption on goethite. *Environ. Sci. Technol.* **2001**, *35*, 3369−3374.

(37) von Wandruszka, R. Phosphorus retention in calcareous soils and the effect of organic matter on its mobility. *Geochem. T.* **2006**, *7*, 6.

(38) Chrysikopoulos, C. V.; Syngouna, V. I. Effect of gravity on colloid transport through water-saturated columns packed with glass beads: modeling and experiments. *Environ. Sci. Technol.* **2014**, *48*, 6805−6813.

(39) Chrysikopoulos, C. V.; Sotirelis, N. P.; Kallithrakas-Kontos, N. G. Cotransport of Graphene Oxide Nanoparticles and Kaolinite Colloids in Porous Media. *Transport Porous Med* **2017**, *119*, 181−204.

(40) Katzourakis, V. E.; Chrysikopoulos, C. V. Modeling the Transport of Aggregating Nanoparticles in Porous Media. *Water Resour. Res.* **2021**, *57*, No. e2020WR027946.

(41) Wu, M.; Bi, E.; Li, B. Cotransport of nano-hydroxyapatite and different Cd(II) forms influenced by fulvic acid and montmorillonite colloids. *Water Res.* **2022**, *218*, 118511.

(42) Chotpantarat, S.; Kiatvarangkul, N. Facilitated transport of cadmium with montmorillonite KSF colloids under different pH conditions in water-saturated sand columns: Experiment and transport modeling. *Water Res.* **2018**, *146*, 216−231.

(43) Hiemstra, T.; Van Riemsdijk, W. H. Surface structural ion adsorption modeling of competitive binding of oxyanions by metal (Hydr)oxides. *J. Colloid Interface Sci.* **1999**, *210*, 182−193.

(44) Antelo, J.; Arce, F.; Fiol, S. Arsenate and phosphate adsorption on ferrihydrite nanoparticles. Synergetic interaction with calcium ions. *Chem. Geol.* **2015**, *410*, 53−62.

(45) Tiberg, C.; Gustafsson, J. P. Phosphate effects on cadmium(II) sorption to ferrihydrite. *J. Colloid Interface Sci.* **2016**, *471*, 103−111.

(46) Antelo, J.; Fiol, S.; Pérez, C.; Mariño, S.; Arce, F.; Gondar, D.; López, R. Analysis of phosphate adsorption onto ferrihydrite using the CD-MUSIC model. *J. Colloid Interface Sci.* **2010**, *347*, 112−119.

(47) Lu, T.; Manzetti, S. Wavefunction and reactivity study of benzo[a]pyrene diol epoxide and its enantiomeric forms. *Struct. Chem.* **2014**, *25*, 1521−1533.

(48) Jia, Y. F.; Xu, L. Y.; Wang, X.; Demopoulos, G. P. Infrared spectroscopic and X-ray diffraction characterization of the nature of adsorbed arsenate on ferrihydrite. *Geochim. Cosmochim. Ac.* **2007**, *71*, 1643−1654.

(49) Ma, J.; Guo, H.; Weng, L.; Li, Y.; Lei, M.; Chen, Y. Distinct effect of humic acid on ferrihydrite colloid-facilitated transport of arsenic in saturated media at different pH. *Chemosphere* **2018**, *212*, 794−801.

(50) Bradford, S. A.; Simunek, J.; Bettahar, M.; van Genuchten, M. T.; Yates, S. R. Modeling colloid attachment, straining, and exclusion in saturated porous media. *Environ. Sci. Technol.* **2003**, *37*, 2242−2250.

(51) Yu, B.; Jia, S. Y.; Liu, Y.; Wu, S. H.; Han, X. Mobilization and re-adsorption of arsenate on ferrihydrite and hematite in the presence of oxalate. *J. Hazard. Mater.* **2013**, *262*, 701−708.

(52) Verwey, E. J. W.; Overbeek, J. T. G. *Theory of the Stability of Lyophobic Colloids*; ElsevierThe Netherlands: Amsterdam, 1948, pp 224−225.

(53) Derjaguin, B.; Landau, L. Theory of the stability of strongly charged lyophobic sols and of the adhesion of strongly charged particles in solutions of electrolytes. *Acta Physicochim. URSS* **1941**, *14*, 733−76230.

(54) Frisch, M. J.; Trucks, G. W.; Schlegel, H. B.; Scuseria, G. E.; Robb, M. A.; Cheeseman, J. R.; Scalmani, G.; Barone, V.; Petersson, G. A.; Nakatsuji, H.; Li, X.; Caricato, M.; Marenich, A. V.; Bloino, J.; Janesko, B. G.; Gomperts, R.; Mennucci, B.; Hratchian, H. P.; Ortiz, J. V.; Izmaylov, A. F.; Sonnenberg, J. L.; Williams-Young, D.; Ding, F.; Lipparini, F.; Egidi, F.; Goings, J.; Peng, B.; Petrone, A.; Henderson, T.; Ranasinghe, D.; Zakrzewski, V. G.; Gao, J.; Rega, N.; Zheng, G.; Liang, W.; Hada, M.; Ehara, M.; Toyota, K.; Fukuda, R.; Hasegawa, J.; Ishida, M.; Nakajima, T.; Honda, Y.; Kitao, O.; Nakai, H.; Vreven, T.; Throssell, K.; Montgomery, J. A., Jr.; Peralta, J. E.; Ogliaro, F.; Bearpark, M. J.; Heyd, J. J.; Brothers, E. N.; Kudin, K. N.; Staroverov, V. N.; Kobayashi, R.; Normand, J.; Raghavachari, K.; Rendell, A. P.; Burant, J. C.; Iyengar, S. S.; Tomasi, J.; Cossi, M.; Millam, J. M.; Klene, M.; Adamo, C.; Cammi, R.; Ochterski, J. W.; Martin, R. L.; Morokuma, K.; Farkas, O.; Foresman, J. B.; Fox, D. J. *Gaussian 16, Revision B.01*; Gaussian, Inc.: Wallingford CT, 2016.

(55) Lu, T.; Chen, F. Multiwfn: a multifunctional wavefunction analyzer. *J. Comput. Chem.* **2012**, *33*, 580−592.

(56) Christen, M.; Hünenberger, P. H.; Bakowies, D.; Baron, R.; Bürgi, R.; Geerke, D. P.; Heinz, T. N.; Kastenholz, M. A.; Kräutler, V.; Oostenbrink, C.; Peter, C.; Trzesniak, D.; van Gunsteren, W. F. The GROMOS software for biomolecular simulation: GROMOS05. *J. Comput. Chem.* **2005**, *26*, 1719−1751.

(57) Canzar, S.; El-Kebir, M.; Pool, R.; Elbassioni, K.; Malde, A. E.; Mark, D. P.; Geerke, L.; Stougie, G. W.; Klau, G. W. Charge group partitioning in biomolecular simulation. *J. Comput. Biol.* **2013**, *20*, 188−198.

(58) Hess, B.; Kutzner, C.; van der Spoel, D.; Lindahl, E. GROMACS 4: Algorithms for Highly Efficient, Load-Balanced, and Scalable Molecular Simulation. *J. Chem. Theory Comput.* **2008**, *4*, 435−447.

(59) Sun, P.; Shijirbaatar, A.; Fang, J.; Owens, G.; Lin, D.; Zhang, K. Distinguishable transport behavior of zinc oxide nanoparticles in silica sand and soil columns. *Sci. Total Environ.* **2015**, *505*, 189−198.

(60) Ma, J.; Qiu, Y.; Zhao, J.; Ouyang, X.; Zhao, Y.; Weng, L.; MD Yasir, M. A.; Chen, Y.; Li, Y. Effect of agricultural organic inputs on nanoplastics transport in saturated goethite-coated porous media: Particle size selectivity and role of dissolved organic matter. *Environ. Sci. Technol.* **2022**, *56*, 3524−3534.

(61) Xu, S.; Chen, X.; Zhuang, J. Opposite influences of mineral-associated and dissolved organic matter on the transport of hydroxyapatite nanoparticles through soil and aggregates. *Environ. Res.* **2019**, *171*, 153−160.

(62) Cornelis, G.; Pang, L.; Doolette, C.; Kirby, J. K.; McLaughlin, M. J. Transport of silver nanoparticles in saturated columns of natural soils. *Sci. Total Environ.* **2013**, *463-464*, 120−130.

(63) Yang, W.; Bradford, S. A.; Wang, Y.; Sharma, P.; Shang, J.; Li, B. Transport of biochar colloids in saturated porous media in the presence of humic substances or proteins. *Environ. Pollut.* **2019**, *246*, 855−863.

(64) McCarthy, J. F.; McKay, L. D.; Bruner, D. D. Influence of ionic strength and cation charge on transport of colloidal particles in fractured shale saprolite. *Environ. Sci. Technol.* **2002**, *36*, 3735−3743.

(65) Bradford, S. A.; Torkzaban, S.; Walker, S. L. Coupling of physical and chemical mechanisms of colloid straining in saturated porous media. *Water Res.* **2007**, *41*, 3012−3024.

(66) Lin, J.; Zhan, Y.; Wang, H.; Chu, M.; Wang, C.; He, Y.; Wang, X. Effect of calcium ion on phosphate adsorption onto hydrous zirconium oxide. *Chem. Eng. J.* **2017**, *309*, 118−129.

(67) Li, J.; Weng, L.; Deng, Y.; Ma, J.; Chen, Y.; Li, Y. NOM-mineral interaction: Significance for speciation of cations and anions. *Sci. Total Environ.* **2022**, *820*, 153259.

(68) Kumar, A. A.; Som, A.; Longo, P.; Sudhakar, C.; Bhuin, R. G.; Gupta, S. S.; Anshup; Sankar, M. U.; Chaudhary, A.; Kumar, R.; Pradeep, T. Confined metastable 2-line ferrihydrite for affordable point-of-use arsenic-free drinking water. *Adv. Mater.* **2017**, *29*, 1604260.

(69) Cui, H.; Yang, X.; Xu, L.; Fan, Y.; Yi, Q.; Li, R.; Zhou, J. Effects of goethite on the fractions of Cu, Cd, Pb, P and soil enzyme activity with hydroxyapatite in heavy metal-contaminated soil. *RSC Adv.* **2017**, *7*, 45869−45877.

(70) Wang, X.; Hu, Y.; Tang, Y.; Yang, P.; Feng, X.; Xu, W.; Zhu, M. Phosphate and phytate adsorption and precipitation on ferrihydrite surfaces. *Environ. Sci. Nano* **2017**, *4*, 2193−2204.

(71) Mendez, J. C.; Hiemstra, T. Carbonate adsorption to ferrihydrite: Competitive interaction with phosphate for use in soil systems. *ACS Earth Space Chem* **2019**, *3*, 129−141.

(72) Kubicki, J. D.; Paul, K. W.; Kabalan, L.; Zhu, Q.; Mrozik, M. K.; Aryanpour, M.; Pierre-Louis, A. M.; Strongin, D. R. ATR-FTIR and density functional theory study of the structures, energetics, and vibrational spectra of phosphate adsorbed onto goethite. *Langmuir* **2012**, *28*, 14573−14587.

(73) Parr, R. G.; Donnelly, R. A.; Levy, M.; Palke, W. E. Electronegativity: The density functional viewpoint. *J. Chem. Phys.* **1978**, *68*, 3801−3807.

(74) Zhang, M.; Bradford, S. A.; Klumpp, E.; Šimůnek, J.; Wang, S.; Wan, Q.; Jin, C.; Qiu, R. Significance of Non-DLVO Interactions on the Co-Transport of Functionalized Multiwalled Carbon Nanotubes and Soil Nanoparticles in Porous Media. *Environmental science & technology* **2022**, *56*, 10668−10680.

(75) Weng, L.; Van Riemsdijk, W. H.; Koopal, L. K.; Hiemstra, T. Ligand and Charge Distribution (LCD) model for the description of fulvic acid adsorption to goethite. *J. Colloid Interface Sci.* **2006**, *302*, 442−457.

(76) Stumm, W.; Morgan, J. J. *Aquatic Chemistry: An Introduction Emphasizing Chemical Equilibrium in Natural Waters*; Wiley: New York, 1981, p 796.

(77) Brown, M. A.; Abbas, Z.; Kleibert, A.; Green, R. G.; Goel, A.; May, S.; Squires, T. M. Determination of surface potential and electrical double-layer structure at the aqueous electrolyte-nanoparticle interface. *Phys. Rev. X* **2016**, *6*, 011007.

(78) Rahnemaie, R.; Hiemstra, T.; van Riemsdijk, W. H. Geometry, charge distribution, and surface speciation of phosphate on goethite. *Langmuir* **2007**, *23*, 3680−3689.

(79) Styles, D.; Coxon, C. Laboratory drying of organic-matter rich soils: Phosphorus solubility effects, influence of soil characteristics, and consequences for environmental interpretation. *Geoderma* **2006**, *136*, 120−135.

(80) Grolimund, D.; Borkovec, M. Colloid facilitated transport of strongly sorbing contaminants in natural porous media: mathematical modeling and laboratory column experiments. *Environ. Sci. Technol.* **2005**, *39*, 6378−6386.

(81) Massoudieh, A.; Ginn, T. R. Modeling colloid-facilitated transport of multi-species contaminants in unsaturated porous media. *J. Contam. Hydrol.* **2007**, *92*, 162−83.

(82) Tang, X. Y.; Weisbrod, N. Colloid-facilitated transport of lead in natural discrete fractures. *Environ. Pollut.* **2009**, *157*, 2266−74.

(83) Tran, E.; Zavrin, M.; Kersting, A. B.; Klein-BenDavid, O.; Teutsch, N.; Weisbrod, N. Colloid-facilitated transport of (238)Pu, (233)U and (137)Cs through fractured chalk: Laboratory experiments, modelling, and implications for nuclear waste disposal. *Sci. Total Environ.* **2021**, *757*, 143818.

(84) Ling, X.; Yan, Z.; Liu, Y.; Lu, G. Transport of nanoparticles in porous media and its effects on the co-existing pollutants. *Environ. Pollut.* **2021**, *283*, 117098.

(85) Wang, Y.; Ouyang, W.; Lin, C.; Zhu, W.; Critto, A.; Tysklind, M.; Wang, X.; He, M.; Wang, B.; Wu, H. Higher fine particle fraction in sediment increased phosphorus flux to estuary in restored Yellow River Basin. *Environ. Sci. Technol.* **2021**, *55*, 6783−6790.